RSC Advances

PAPER

View Article Online
View Journal | View Issue

Cite this: *RSC Adv.*, 2025, **15**, 47410

Engineered flower-like hierarchical Cu_2S architectures mediated by carbon nanotubes and Ti_3C_2 for enhanced ionic diffusion and charge carriers in hybrid supercapacitors

Manzoor Khan,[a] Muhammad Luqman,[a] Muhammad Mehak,[a] Muhammad Ishaq,[a] Asif Mahmood,[b] Waheed Al-Masry,[b] Mahmood Nawaz[c] and Shahid Atiq *[a]

Growing global energy demands have stimulated extensive efforts toward sustainable energy solutions. In this work, Cu_2S (CS) and its composites (CS-CNTs and CS-MXene) were studied for advanced supercapacitor devices. Surface analysis revealed a flower-like hierarchical architecture with high porosity, as evident by Brunauer–Emmett–Teller analysis, providing abundant active sites and promoting fast ion transport. Dunn's model analysis revealed a hybrid charge-storage behavior of all the prepared electrode materials. Among all prepared electrodes, the CS/MXene demonstrated the most superior electrochemical features in half-cell analysis, exhibiting a specific capacity (C_{sc}) of 1692C g^{-1} with an impressive energy density (E_d) of 112 Wh kg^{-1} at a current density (I_d) of 11.7 A g^{-1}. Upon full-cell analysis, the CS/MXene composite delivered a remarkable C_{sc} of 371.63C g^{-1} at I_d of 3.13 A g^{-1}, with E_d of 61.93 Wh kg^{-1} at P_d of 1882.35. Furthermore, the CS/MXene retained 97.5% of its initial capacity after 5000 consecutive charge/discharge cycles. Furthermore, the electrode exhibited the shortest relaxation time, moderate diffusion coefficient and the highest ionic conductivity (0.092 S cm^{-1}), confirming its superior charge transport efficiency compared to other electrodes. Collectively, these results highlight the potential of these materials for high-performance hybrid supercapacitors.

Received 4th October 2025
Accepted 18th November 2025

DOI: 10.1039/d5ra07565c

rsc.li/rsc-advances

1. Introduction

In the contemporary technological era, rapid advancements in high-tech industries are intrinsically linked to escalating environmental concerns. The extensive reliance on fossil fuels has resulted in a significant increase in emissions of hazardous gases, unpredictable climatic fluctuations, accelerated discharge of chemical pollutants, and imbalanced global energy distribution.[1–3] To mitigate these impending ecological crises, the fabrication of flexible, non-polluting, and cost-effective energy storage devices (ESDs) has become an urgent necessity. In this context, green energy technologies have garnered substantial interest from the scientific community, particularly within the domain of renewable energy research.[4] There is a growing demand for flexible, clean, and efficient ESDs capable of storing energy from sustainable sources. In this context, electrochemical (EC) energy storage systems, particularly fuel cells, supercapacitors (SCs) and batteries, have emerged as promising candidates. As compared to batteries, SCs acquired noteworthy importance due to extraordinary specific capacitance (C_s), quick charge/discharge rate, phenomenal power density (P_d), and long-lasting life cycles.[5–7] On the basis of the charge storage response, SCs are categorized into three major types. The type of SCs that store charge electrostatically at the interface of electrode/electrolyte (*E*/*E*) *via* non-faradaic reactions are named as electric double layer capacitors (EDLCs) and are well known for their superior P_d and long life cycle.[8,9] In contrast, SCs that store charge *via* fast and reversible faradaic redox reactions are classified as pseudocapacitors, which are distinguished by their notable energy density (E_d).[10] Another class of SCs, known as hybrid capacitors, integrates the charge storage mechanism of both EDLCs and pseudocapacitors, and the charge storage process depends upon the faradaic as well as non-faradaic processes.[5] Hybrid capacitors, which have three further types named as composite, asymmetric, and battery-type capacitors, each offering unique structural and EC advantages.[3,7]

In the past few years, noteworthy research has centered around the utilization of versatile, flexible, and cost-effective electrode materials for the fabrication of SCs. A wide range of materials, including nitrides, carbides, transition metal oxides (TMOs), and metal sulfides, have been explored for this

[a]*Centre of Excellence in Solid State Physics, University of the Punjab, Lahore-54590, Pakistan. E-mail: satiq.cssp@pu.edu.pk*

[b]*College of Engineering, Chemical Engineering Department, King Saud University, 11421, Riyadh, Saudi Arabia*

[c]*Centre for Ultrafast Phase Transformation, Department of Physics, Sogang University, Seoul 04107, Korea*

purpose. Researchers discovered that the different metal sulfides (MS), such as lead sulfide (PbS), manganese sulfide (MnS), zinc sulfide (Zn_2S), and copper sulfide (Cu_2S), have emerged as promising candidates owing to their availability, cost-effectiveness, and extraordinary $C_{s,}$ and are well known for their rapid redox reaction.[11–14] In particular, Cu_2S (CS) has attracted considerable attention as a potential electrode material due to its specific capacity (C_{sc}), excellent thermal and EC stability, multiple oxidation states, low cost, wide availability, and favorable intercalation behavior. However, the practical application of CS is hindered by its inherently low electrical conductivity, which remains a critical factor limiting its EC performance in SC devices.[9,15]

Numerous studies have investigated CS for a variety of applications, with several notable examples highlighted in the present work. A combustion technique was used by Mirzanlou *et al.* for the synthesis of CS nanoparticles (NPs), where nickel foam (NF) was used as a substrate.[16] At a current density (I_d) of 1 A g^{-1}, CS displayed an excellent C_s of 677 F g^{-1}. The synthesized hybrid SCs device (CS//MnO_2), in which CS served as the cathode and MnO_2 was taken as anode, revealed the superior E_d of 42.31 Wh kg^{-1} at I_d of 1 A g^{-1}. Moreover, the device showed 86.02% of the initial C_s after 6500 cycles, at I_d of 3 A g^{-1}. Similarly, Das *et al.* successfully synthesized CS//NiS//Ni_3S_4 nanocomposite *via* the hydrothermal route.[17] CS//NiS//Ni_3S_4 revealed the C_{sc} of 363.06 mA h g^{-1} at I_d of 0.5 A g^{-1} and, after 8000 cycles, showed the retention rate of 94.8%. Asymmetric SCs assembly exhibited a C_{sc} of 55.08 mA h g^{-1} and the E_d of 41.53 Wh kg^{-1} at 1 A g^{-1}. Hydrothermal route was adopted by Duan *et al.* for the synthesis of CS//C@NiMnCe-LDH (layered double hydroxide) composites on copper foam (CF) with superior morphology.[18] CS//C@NiMnCe-LDH/CF attained an aerial capacitance of 5176.5 mF cm^{-2} at I_d of 2 mA cm^{-2}. The fabricated asymmetric SCs device showed a remarkable mass capacitance of 150.83 F g^{-1} while possessing superior E_d and P_d of 53.63 Wh kg^{-1} and 640 W kg^{-1}, respectively. Similarly, Tian *et al.* used a continuous synthesis route for the synthesis of CS//$NiFe_2S$ nanorods in which CF was taken as a substrate.[19] CS//$NiFe_2S$ revealed a superior C_{sc} of 588.02 mA h g^{-1} at I_d of 1 A g^{-1}. An asymmetric SC device was fabricated by the assembling of CS//$NiFe_2S$/CF/AC, which exhibited an E_d of 68.61 Wh kg^{-1} and a P_d of 800.01 W kg^{-1}. Recently, Rani *et al.* successfully prepared the NPs of CuS//CS as well as CuS//CS//MWCNTs nanocomposite with the help of the hydrothermal route.[20] CuS//CS and CuS//Cu_2S//MWCNTs displayed an exceptional C_{sc} of 357 and 427.3 mA h g^{-1}, respectively, at I_d of 1 A g^{-1}. An asymmetric SC device was fabricated by the assembly of CuS//CS//MWCNTs and activated carbon (AC), which exhibits a noteworthy E_d of 70.01 Wh kg^{-1} while possessing an excellent P_d of 750 W kg^{-1}.

Considering the aforementioned studies, a primary challenge that has been prioritized is the development of electrode material exhibiting extended cyclic life alongside enhanced EC performance. To address these challenges, further improvement in the EC properties of carbon-based structures is imperative to meet the increasing energy crisis. In the present challenging scenario, carbon nanotubes (CNTs) and MXene (Ti_3C_2) have appeared as emerging co-materials for the synthesis of composite electrode material based on CS, owing to their exceptional electrical conductivity.[21,22] These synergistic properties render CS-based composites as highly competent electrode materials for practical implementation in SC applications.

In the present study, CS was synthesized *via* an eco-friendly hydrothermal method, employing porous NF as the substrate. The primary objective of this work was the development of an electrode material with a high density of EC active sites to facilitate efficient *E*/*E* interactions, thereby enhancing the EC performance of SCs. To achieve this objective, CS was initially incorporated with 10% CNTs to form the CS-CNTs composite. Subsequently, CS was integrated with 10% MXene to synthesize the CS-MXene hybrid. Among all synthesized samples, the CS-MXene composite demonstrated superior EC performance, characterized by enhanced E_d, remarkable P_d, and excellent cycling stability. An in-depth analysis of the diffusion dynamics was conducted to elucidate the underlying ion-transport behaviour governing the electrode performance. These attributes underscore its potential as a promising electrode material for high-performance SCs.

2. Experimental section

2.1 Synthesis of CS

To synthesize the pure phase of CS, a hydrothermal method was employed, as illustrated in Fig. 1. Copper nitrate and thiourea were used as precursors, which were dissolved in 45 mL of deionized (DI) water in a beaker. The resulting solution was first sonicated in an ultrasonic bath for 30 min to ensure proper dispersion, followed by magnetic stirring at 250 rpm for another 30 min to achieve complete dissolution of the reactant. This process yielded a clear and homogeneous precursor solution, ready for hydrothermal processing. For the heat treatment, the precursor solution was transferred into an autoclave and placed in a muffle furnace at 150 °C for 18 h. After naturally cooling to room temperature (RT), the resulting precipitates were collected and washed several times with ethanol and DI water. Finally, the washed product was dried in an oven to obtain a fine, uniform powder for further characterization.

2.2 Synthesis of CS/CNTs and CS/MXene composites

Two composites were synthesized by incorporating 10% MXene with 90% CS and 10% CNTs with 90% CS, respectively. Initially, the materials were dispersed in 45 mL DI water, followed by sonication and magnetic stirring for 30 min to ensure thorough mixing and immersion of the composite phases. The resulting mixtures were then transferred into Teflon-lined autoclave cylinders. The autoclaves were heated in furnaces at 100 °C for 2 h, after which they were allowed to cool naturally to room temperature. The obtained samples were washed several times using ethanol and DI water to remove any impurities. Finally, the wet composites were dried in an oven to eliminate residual moisture, yielding fine, homogeneous powders ready for EC analysis.

Fig. 1 Schematic illustration of the synthesis method and electrode material fabrication process.

2.3 Preparation of electrodes

For the preparation of the WE, nickel foam (NF) with dimensions 1 × 1.25 cm^2 was first etched using hydrochloric acid (HCl) and DI water solution in a volume ratio of 1 : 3. The NF was sonicated in this solution for 30 min. After etching, it was thoroughly rinsed by sonicating in 50 mL of DI water for another 30 min to completely remove any residual acid and surface impurities. The cleaned NF was then dried in an oven at 70 °C for several min. Next, a slurry was prepared by mixing 85% of active material with 5% activated carbon (AC) and 10% binder to enhance adhesion. To ensure uniform dispersion, the slurry tubes were placed on a magnetic stirrer at 250 rpm for 8 h. Finally, the resulting homogeneous slurry was drop-casted onto the pretreated NF using a micropipette, with an active material of approximately 1 ± 0.1% mg cm^{-2} on each electrode.

3. Characterization techniques

Structural analysis was carried out using a Bruker D8 Advance X-ray diffractometer (XRD), enabling determination of phase composition and crystallographic parameters. The morphological features were examined using a Nova-Nano SEM-450 scanning electron microscope (SEM), while surface textural properties were further determined using a Tristar-II 3020 analyzer, through the Brunauer–Emmett–Teller (BET) method. An Oxford Instrument energy dispersive X-ray spectroscopy (EDX) was employed to examine the elemental composition. EC interpretation contributes a pivotal role in analyzing the electrical capabilities, charge storage mechanisms of synthesized samples, and in appraising their service in ESDs of prepared samples.[23,24] For the evaluation of EC characterization of prepared samples, measurements were conducted using a CHI 660 EC workstation in half and full-cell configurations. In this setup, the WE consisted of all synthesized samples, the Pt wire functioned as a CE, and an Ag/AgCl electrode was employed as the RE.[25,26] Throughout the EC investigations, 1 M potassium hydroxide (KOH) was employed as the electrolyte owing to superior ionic conductivity as well as superior chemical stability. For the evaluation of EC performance of the prepared samples, cyclic voltammetry (CV), galvanostatic charge–discharge (GCD), and electrochemical impedance spectroscopy (EIS) tests were conducted. Moreover, for the exploration of the diffusion dynamics of all the synthesized samples, the galvanostatic intermittent titration technique (GITT) was employed.

4. Results and discussion

4.1 Structural analysis

XRD analysis was employed to confirm the crystal structure of the synthesized samples. The XRD patterns of all prepared materials are presented in Fig. 2(a), demonstrating distinct and sharp diffraction peaks, which indicate the high crystallinity and structural integrity of the samples. The orthorhombic crystal structure was confirmed by the XRD pattern for CS, well matched with the ICSD card no. 00-023-0961. The diffracted peaks for CS at 2θ values of 22.9°, 27.96°, 29.3°, 30.7°, 31.85°, 33.48°, 34.5°, 35.75°, 36.63°, 37.83°, 42.37°, 43.48°, 45.53°, 47.91°, 53.1°, and 59.8° were indexed as (242), (420), (243), (091), (191), (224), (353), (423), (433), (1 11 1), (225), (444), (199), (2 13 1), (662), (406) and (486) planes, respectively. Fig. 2(b) depicts the orthorhombic crystal structure of the prepared material. In the XRD pattern of the CS-CNTs composite, no additional

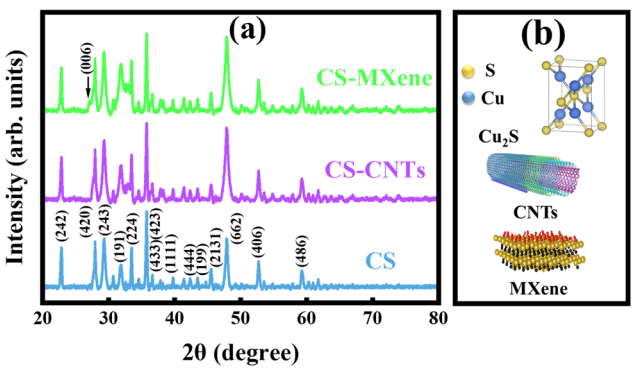

Fig. 2 (a) XRD patterns of CS, CS-CNTs, and CS-MXene, and (b) crystal structure of CS and structures of CNTs and MXene.

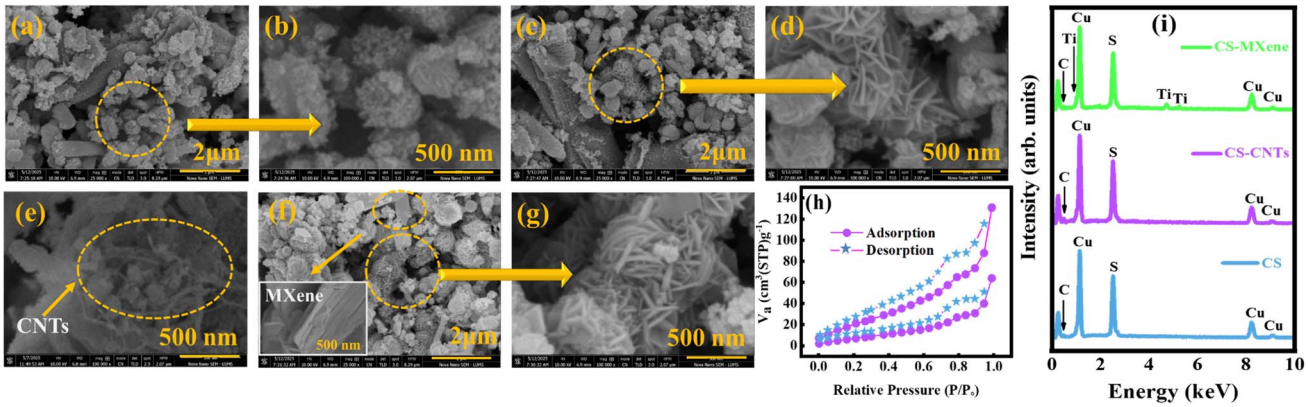

Fig. 3 (a and b) SEM images of CS, (c–e) CS-CNTs, and (f and g) CS-MXene at different magnifications, (h) BET analysis of CS and CS-MXene, and (i) EDX spectra displaying elemental composition of all the prepared samples.

diffraction peaks were observed due to the amorphous nature of CNTs. In contrast, a subtle shoulder peak was observed in the CS-MXene pattern at 2θ value of 27.94° corresponding to the (006) plane, which confirmed the incorporation of MXene into the composite structure.[27] Overall, the crystallinity of the CS phase in all the samples remained intact.

The crystallite size of all the samples was calculated using Scherrer's formula as given in eqn (1).[28,29]

$$D = \frac{0.94\lambda}{\beta \cos \theta} \quad (1)$$

In the above equation, λ denotes the wavelength, β corresponds to the full width at half maximum, and θ is the diffraction angle. Using this relation, the calculated crystallite sizes for CS, CS-CNTs, and CS-MXene were 33.2, 26.6, and 27.2 nm, respectively. The lattice strain values for CS, CS-CNTs, and CS-MXene were determined to be 0.172, 0.261, and 0.278, respectively. These results confirmed the successful synthesis of the CS phase and its composites.

4.2 Morphological analysis

SEM was employed for the morphological analysis of synthesized materials. Morphological analysis provides critical insights into particle shape, size, and spatial distribution across the material's surface, all of which play a significant role in influencing the EC performance of electrode material.[30] Fig. 3(a and b) shows spherical-shaped particles for CS, which are distributed randomly. In addition, SEM images revealed the hierarchical architecture of CS with a flower-shaped structure, which has a profound impact on the EC properties of the synthesized samples. SEM images of the CS-CNTs composite revealed a preserved flower-like morphology, similar to that observed for pristine CS, as depicted in Fig. 3(c–e). Additionally, tubular structures corresponding to CNTs are visibly attached to the special flower-like particles, confirming the successful incorporation of CNTs. The presence of these tubular features contributes to enhanced porosity as well as electrical conductivity, thereby improving the EC performance of the composite. Fig. 3(f and g) displayed the SEM micrographs of the CS-MXene composite, which exhibited a distinct layered morphology indicative of successful MXene integration. The characteristic flower-like structure was also retained. The synergistic combination of the layered architectures and flower-like morphology leads to an increased surface area and improved porosity. Moreover, the CS structures exhibited multi-petaled flower-like formations with petals extending in various directions and interconnecting with one another, resulting in an open and porous network favorable for EC applications. The open porous morphology observed in the samples is expected to offer an abundance of active sites for ion intercalation/deintercalation processes, thereby increasing the effective surface area, an essential factor for enhancing EC performance.[31] These features also facilitate improved charge transport kinetics and enhance electron (e^-) conductivity. Furthermore, the incorporation of MXene contributes to the uniform dispersion of CS particles across its structure. It also modulates the interlayer spacing and enhances interfacial contact at the *E*/*E* interface, both of which are critical parameters for optimizing the EC properties of the electrode material.

4.3 BET surface analysis

To determine the EC performance of electrode materials, the surface area, pore volume, and pore size distribution play an important role. A large surface area facilitates more active sites for charge storage; on the other hand, the desired pore morphology provides fast ion intercalation and ensures transportation of electrolyte to the internal pores of the electrode's materials. Generally, micropores facilitate charge storage, mesopores contribute to fast ion diffusion, and macropores serve as buffering channels that reduce resistance during the charge–discharge process. BET analysis was conducted to differentiate these morphological features, as it provides qualitative information about the textural parameters of the testing electrodes, which directly influence the charge kinetics and overall EC efficiency of electrode materials. In this technique, nitrogen (N_2) gas was taken inside the surface of the electrode by enhancing the pressure; as a result, the adsorption curve

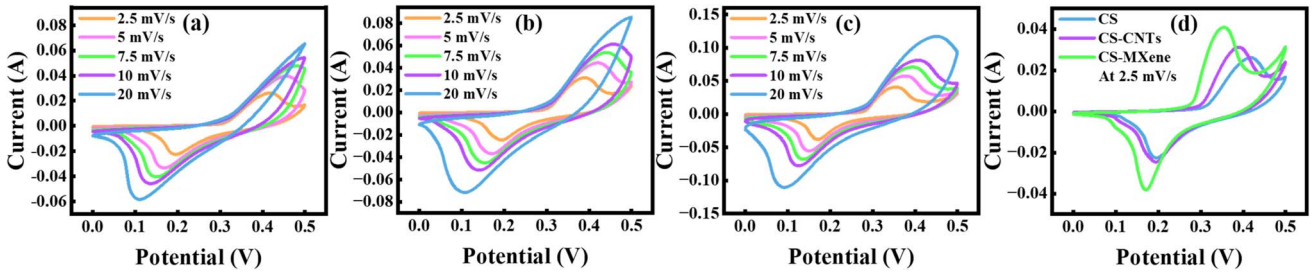

Fig. 4 (a–c) Cyclic voltammograms of CS, CS-CNTs, and CS-MXene, and (d) comparison of CV profiles of all the synthesized samples at a scan rate of 2.5 mV s^{-1}.

obtained was used to estimate the surface area and pore volume of the electrode materials. As pressure decreased, the N_2 gas left the pores of the electrode materials, resulting in a desorption curve which is further analyzed by the Barrett–Joyner–Halenda (BJH) rule to determine the pore size distribution and average pore size.[32,33] Fig. 3(h) shows the N_2 adsorption–desorption profiles of CS and CS-MXene composite along with their pore size distribution. The estimated surface area of CS and CS-MXene composite was found to be 45.27 and 64.18 m^2 g^{-1}, respectively. The CS-MXene composite showed a large surface area, which can enhance its EC efficiency. The development of the monolayer was indicated by the linear enhancement in N_2 adsorption at relatively low pressure (P/P_0 = 0.0–0.1). The relative pore volume for CS and CS-MXene composite was calculated to be 0.37 and 0.28 cm^3 g^{-1}, respectively, which facilitates remarkable ion diffusion.

4.4 Compositional analysis

EDX is a well-known technique for identifying and quantifying the elemental composition of samples, capable of detecting elements with high sensitivity. Fig. 3(i) represents the EDX spectra for CS, CS-CNTs, and CS-MXene, which revealed the existence of copper (Cu), carbon (C), as well as sulfur (S). EDX spectrum of CS revealed no additional peaks, which confirmed the absence of any contamination in the prepared material.[34,35] In the CS-CNTs composite, a slight increase in the intensity of carbon peaks was observed, which validates the incorporation of CNTs in pristine CS. For the CS-MXene composite, the EDX spectrum exhibited an additional peak corresponding to titanium (Ti), along with a significant increase in C intensity, verifying the successful integration of MXene into the CS structure. Furthermore, the absence of any extraneous peaks in the EDX spectrum of CS-MXene suggests a high degree of purity and the absence of unwanted impurities.

4.5 Voltammetric study

CV is a widely employed EC technique used to evaluate the EC behavior of synthesized materials by graphically representing the relationship between current and applied potential. Additionally, this technique facilitates the investigation of the charge storage mechanism by distinguishing between capacitive and diffusion-controlled contributions, as well as assessing the reversibility of the redox process involved.[36–38] The CV profiles of CS, CS-CNTs, and CS-MXene are presented in Fig. 4(a–c), recorded within a potential window of 0 to 0.5 V. CV measurements were conducted at various scan rates of 2.5, 5, 7.5, 10, and 20 mV s^{-1} to investigate the rate-dependent behavior of the samples. Superimposed redox peaks were also observed, confirming the occurrence of faradaic reactions, thereby verifying the hybrid charge storage mechanism of the material. The area enclosed by each voltammogram is directly proportional to the C_{sc}, implying that a larger enclosed area corresponds to a higher C_{sc} value.[39] At lower scan rates, ions have sufficient time to diffuse into the electrode material, facilitating intercalation and redox kinetics. In contrast, at higher scan rates, limited ion diffusion time at the *E*/*E* interface restricted these processes, leading to a lower C_{sc}. At higher scan rates, ions accumulate at the electrode surface for a shorter duration, leading to the formation of a resistive layer that impedes ion diffusion into the electrode material. This hindered diffusion limits the extent of the redox reactions. To overcome this limitation, an additional potential is required in the shift of redox peaks toward higher current values.[40,41]

The presence of distinct oxidation and reduction peaks in the CV curves confirmed the pseudocapacitive nature of the charge storage mechanism in the CS sample. During CV analysis, CS undergoes the following reversible redox reactions.

$$Cu_2S + OH^- \leftrightarrow CuS_2OH + e^-$$

Initially, CS undergoes oxidation in the presence of hydroxide (OH^-) ions, releasing a single e^- and forming an intermediate species, Cu_2S–OH. This reversible redox occurs between the Cu^+ and Cu^{2+} oxidation states within the CS structure.[42] The theoretical capacity of CS was measured as 1213.2C g^{-1} by the relation ($n \times F/3.6 \times M$), where n is the number of electrons transferred per formula unit (2 in our case), F is a constant 96 485C mol^{-1}, and M is the molar mass of the CS. For the MXene, the theoretical capacity depends on the number of factors, like surface functional groups and the number of electrons transferred (1151.4C g^{-1} if n = 2 and 575.6C g^{-1} if n = 1). CNTs provide storage through double-layer formation and depend on the available surface area of the nanotubes. Collectively, these conductive scaffolds can increase the porosity of the pure sample, thereby increasing the number of active sites for charge storage.

The CV profiles illustrated in Fig. 4(b) demonstrate the EC behavior of the CNTs incorporated into CS, recorded at the

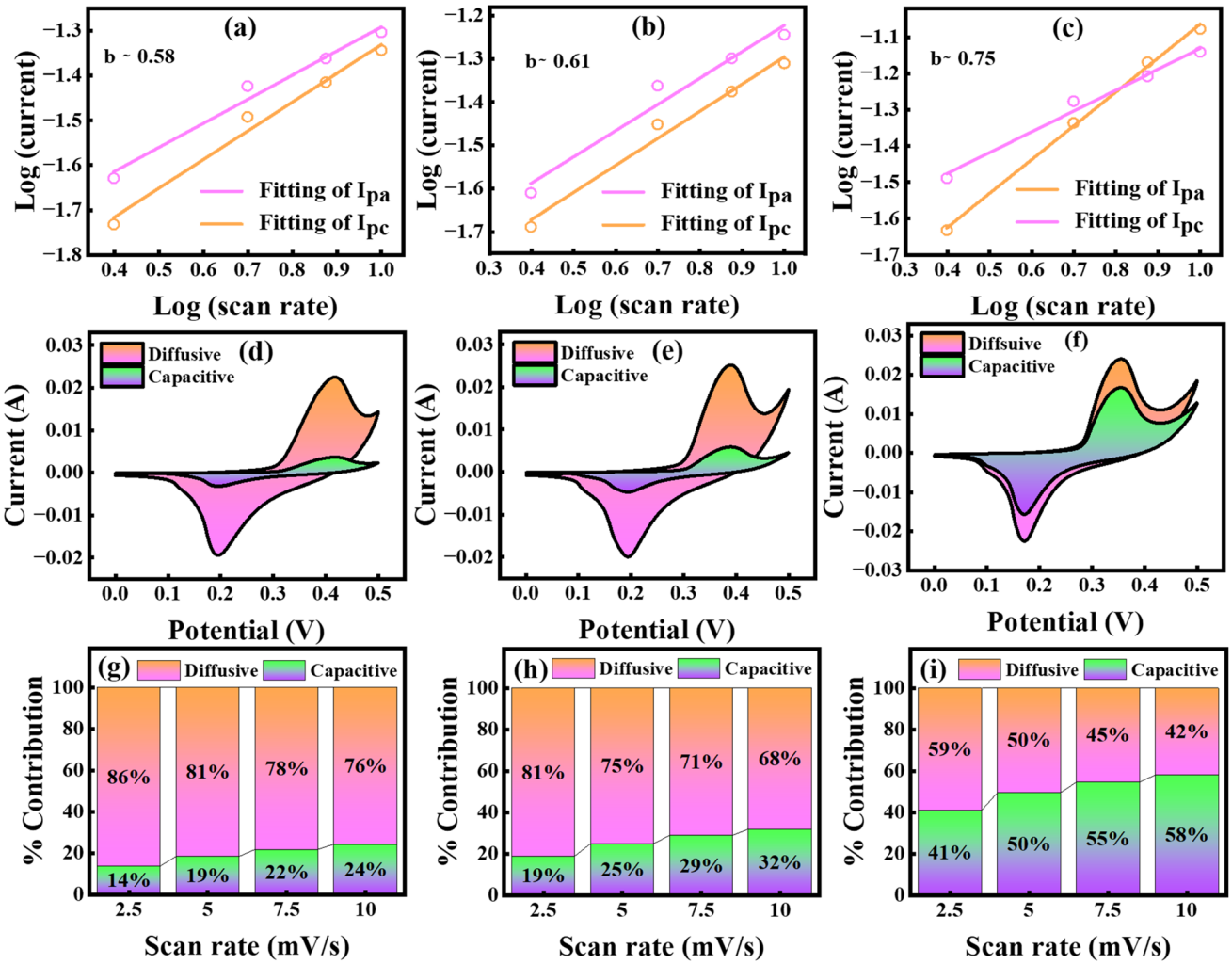

Fig. 5 (a–c) Power's law plots of CS, CS-CNTs, and CS-MXene, (d–f) CV profiles recorded at the lowest scan rate of 2.5 mV s^{-1} showing percentage of capacitive and diffusive current contribution, (g–i) percentage graphs of capacitive and diffusive currents ratios attained from Dunn's plots for all the samples at different scan rates.

same scans as those used for pristine CS. Compared to CS, the CV curves of CS-CNTs displayed a noticeable increase in the enclosed area. This enhancement is attributed to the presence of CNTs, which improve e^- mobility, facilitate ion diffusion, and accelerate charge transfer kinetics. As a result, the electrical conductivity and overall EC performance of the composite are significantly improved. Conversely, Fig. 4(c) presents the CV curves of CS-MXene, highlighting the effect of MXene integration on the EC behavior. Following the integration of MXene, the area enclosed by the CV curves increased significantly compared to those of pristine CS and the CS-CNTs. This enhancement is attributed to the improved morphology, elevated ionic conductivity, and accelerated redox kinetics imparted by MXene, all of which have an important role in boosting EC behavior. Fig. 4(d) presents the CV profiles of all prepared samples recorded at a scan rate of 2.5 mVs^{-1}. Among them, CS-MXene exhibited the largest enclosed area, indicating superior EC characteristics and confirming its potential as high high-performance electrode material.

4.6 Evaluation of charge storage mechanism *via* Dunn's model

The Dunn model is a theoretical framework employed to distinguish between faradaic and non-faradaic charge storage mechanism by analyzing the contributions of diffusion controlled (I_{diff}) and capacitive (I_{cap}) currents, respectively,[43,44] as depicted in Fig. 5. For diffusion controlled (faradaic) processes, the peak currents corresponding to the cathodic (I_{pc}) and anodic (I_{pa}) *versus* the square root of scan rate ($v^{1/2}$) was plotted. In contrast, for capacitive (non-faradaic) processes, the graph was plotted between peak current (I_p) and the scan rate (v).[45–47] The graphical analysis provides valuable insights into the capacitive contribution, EC quality of electrode material, and the classification of the SC system under investigation.[48] CV analysis of the synthesized electrode material demonstrated consistent hybrid charge storage behavior across various scan rates, specifically at 2.5, 5, 7.5, 10, and 20 mV s^{-1}. The model was applied at all above mentioned scan rates, and the corresponding current response was analyzed by plotting current

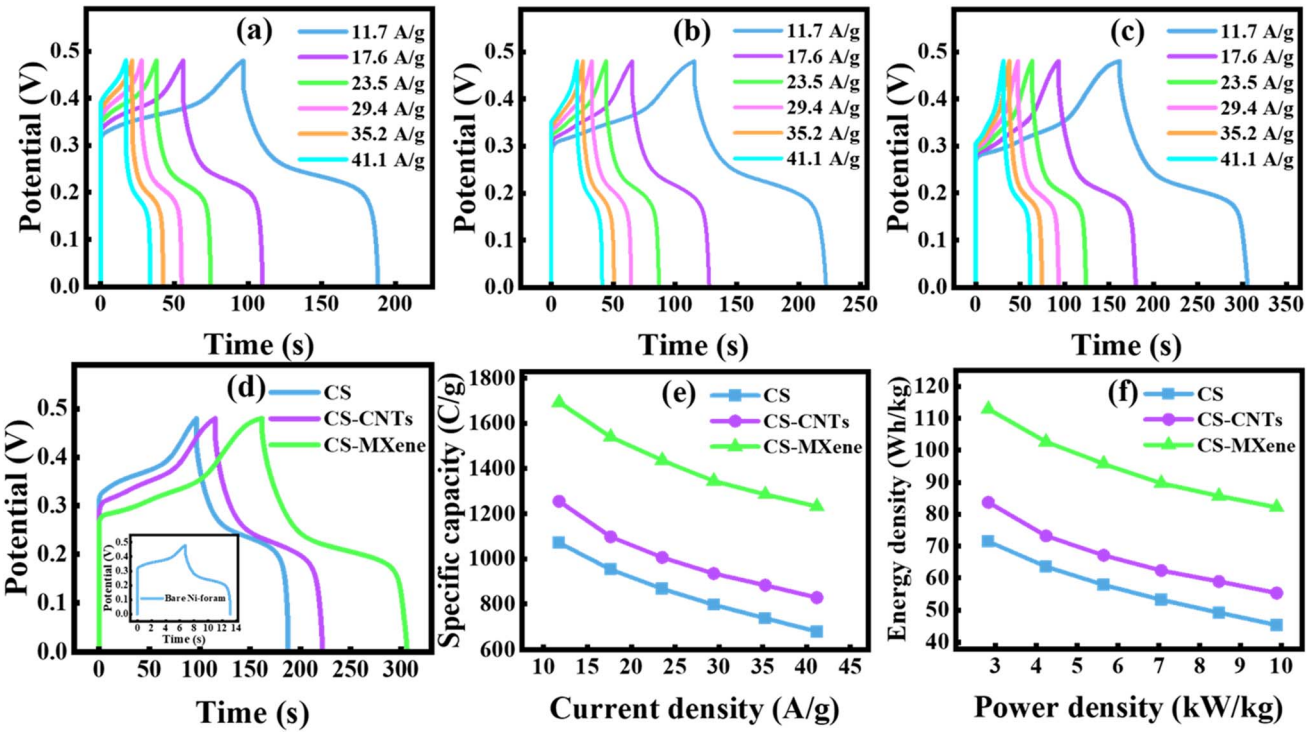

Fig. 6 (a–c) GCD profiles of CS, CS-CNTs, and CS-MXene electrodes, (d) comparison of all prepared samples at 11.7 A g^{-1} current density, (e) variation of specific capacity *vs.* current density, and (f) Ragone plot along with GCD profile of bare Ni foam at same current density.

versus voltage curves. The charge storage mechanism is strongly influenced by both the applied scan rate and I_p. The following power law, given in eqn (2), was utilized to quantify and interpret the charge storage contributions.

$$I_p = av^b \quad (2)$$

In the above equation, peak current (anodic or cathodic) is denoted by I_p, a and b represent the empirical constants, while scan rate is shown by v. The b value was computed by the slope plotting between log(v) and log(I_p), which provides insight into the nature of the charge storage process of synthesized samples. If the b value is near about 0.5, then it demonstrates the diffusion-controlled operation. Conversely, if the b value lies near 1, then it verifies the capacitive operation. A b-value equal to 0.75, which is obtained by the corresponding relationship between log I_p *versus* log v, demonstrates the battery grade behavior of the material.[49–51]

To further elucidate the predominant charge storage operation, the b-values were calculated by fitting the plotted data. For the parent CS sample, a b-value of 0.58 was obtained, as shown

Table 1 Calculated values of specific capacity, energy density, and power density of CS, CS-CNTs and CS-MXene from half-cell GCD analysis

Sample	Current density, (A g^{-1})	Discharge time, (s)	Specific capacity, (C g^{-1})	Energy density, (Wh kg^{-1})	Power density, (W kg^{-1})
CS	11.76	91.03	1070.96	71.39	2823.52
	17.64	54.00	953.08	63.53	4235.29
	23.52	36.86	867.35	57.82	5647.05
	29.41, 35.29	27.11, 20.89	797.39, 737.39	53.15, 49.16	7058.82, 8470.58
	41.17	16.50	679.51	45.30	9882.35
CS-CNTs	11.76	106.71	1255.46	83.69	2823.52
	17.64	62.19	1097.61	73.17	4235.29
	23.52	42.76	1006.7	67.07	5647.05
	29.41, 35.29	31.78, 25.01	934.96, 882.95	62.33, 58.86	7058.82, 8470.58
	41.17	20.12	828.73	55.24	9882.35
CS-MXene	11.76	143.89	1692.88	112.85	2823.52
	17.64	87.20	1538.98	102.59	4235.29
	23.52	61.04	1436.38	95.75	5647.05
	29.41, 35.29	45.74, 36.42	1345.35, 1285.50	89.69, 85.70	7058.82, 8470.58
	41.17	29.92	1232.19	82.14	9882.35

in Fig. 5(a), indicating a hybrid charge storage mechanism with a dominant diffusion-controlled contribution. The CS-CNTs exhibited a slightly higher *b*-value of 0.61, while CS-MXene achieved a *b*-value of 0.75, reflecting an enhanced capacitive contribution as a result of CNTs and MXene integration, shown in Fig. 5(b and c). Dunn's model was also employed to estimate the total current contribution using the following eqn (3)–(5).

$$I_{\text{total}}\,(\text{V}) = I_{\text{Diff}} + I_{\text{Cap}} \tag{3}$$

$$I_{\text{total}} = k_2 v^{1/2} + k_1 v \tag{4}$$

By rearranging the above equation,

$$\frac{I_{\text{total}}(V)}{v^{1/2}} = k_2 + k_1 v^{1/2} \tag{5}$$

In the above equation, total current at constant potential is represented by I_{total} (V),k_1 (capacitive) shows the value of slope, while k_2 (diffusive) displays the value of *y*-intercept obtained after fitting, and v denotes the scan rate. Contribution graphs (capacitive & diffusive) of CS, CS-CNTs, and CS-MXene are displayed in Fig. 5(d–i). At a single scan rate of 2.5 mV s^{-1}, the pristine CS sample exhibited a capacitive contribution of 14% and a dominant diffusive contribution 86%. Under the same conditions, the CS-CNTs demonstrated an increased capacitive contribution of 19% with the remaining 81% attributed to diffusion-controlled processes. Notably, the CS-MXene displayed a significantly enhanced capacitive contribution of 41%, alongside a 59% diffusive contribution, indicating a more surface-driven charge storage dynamics. The enhancement in capacitive behavior observed in CS-CNTs is attributed to the exceptional electrical conductivity of CNTs. The incorporation of CNTs into CS reduces charge transfer resistance (R_{ctr}), thereby enhancing charge carrier kinetics and promoting capacitive performance. Furthermore, CNTs shorten the diffusive path for electrolyte ions and facilitate more efficient ion transport, which also contributes to the observed increase in capacitive contribution. In CS-MXene, the capacitive contribution is significantly enhanced due to the incorporation of MXene, which is well-known for its outstanding electrical conductivity and ability to establish an efficient conductive pathway. This integration facilitates quick redox kinetics and contributes to the improved capacitive behavior. Additionally, the presence of MXene minimizes charge agglomeration at the *E*/*E* interface, thereby increasing the number of accessible active sites for faradaic reactions. Furthermore, the two-dimensional (2D) MXene promotes efficient ion diffusion and enhances electrolyte accessibility, further augmenting capacitive behavior. As the scan rate increases, the residence time of ions at the *E*/*E* interface decreases, which leads to a gradual reduction in diffusion-controlled contribution and a relative increase in capacitive dominance.

4.7 Galvanostatic charge–discharge analysis

GCD testing is a crucial technique for assessing the reversibility and charge/discharge characteristics of the electrode materials, thereby validating their applicability in practical ESDs.[52,53] To comprehensively examine the EC charge storage mechanism, GCD analysis was performed in both half-cell and full-cell configurations, allowing a correlation between the prepared electrode performance and practical device-level behavior. In the three-electrode setup, GCD measurements were carried out within a fixed potential window of 0 to 0.48 V to ensure consistency in EC evaluation. This potential range represents the individual electrode's potential *versus* the reference electrode, and therefore differs from the wider operating voltage observed in the full cell assembly. Fig. 6(a–c) shows the GCD profiles of all the prepared electrode materials in a three-electrode setup. The curves obtained from GCD analysis show a plateau-shaped profile, which determined the existence of redox reactions, reversibility of the electrode materials, and confirmed the hybrid nature of the prepared electrode material. The C_{sc} for the synthesized electrode materials was calculated by using eqn (6).

$$C_{\text{sc}} = \frac{I \times \Delta t}{m} \tag{6}$$

In the above equation, I denotes the current in mA, Δt corresponds to the discharging time in *s*, and m indicates the active mass in mg. Fig. 6(a) presents the GCD profiles of CS, and the values of C_{sc} were computed at different I_{d}. The calculated C_{sc} for CS was calculated to be 1070.96 at I_{d} of 11.7 A g^{-1}. Fig. 6(b) demonstrates the GCD profiles of CS-CNTs, whose values were measured as 1255.4C g^{-1} at a similar I_{d}. On the other hand, Fig. 6(c) displays the CS-MXene GCD profiles and the value of C_{sc} was measured as 1692.8C g^{-1} at the same I_{d}. The calculated values of C_{sc} for all the samples are tabulated in Table 1. A noticeable decrease in discharge time was observed with an increase in I_{d}, which is attributed to the least residence time for the ions at the *E*/*E* interface. At higher I_{d}, ions have insufficient time to diffuse into the EC active sites and instead accumulate at the surface, forming a loosely bound layer. These surface-bound ions can be readily extracted, requiring less time compared to ions that penetrate deeper into the electrode material at lower I_{d}. Fig. 6(d) presents a comparative analysis of GCD profiles for all the prepared samples at least I_{d}. The results indicate that CS-MXene exhibits a notably extended discharge time compared to both CS and CS-CNTs composite. Additionally, the GCD curve of the bare NF was also embedded into Fig. 6(d), exhibiting the minimal charge–discharge contribution of the NF. The enhancement in charge–discharge time was attributed to the incorporation of MXene, highlighting the beneficial role of these additives. The integration of MXene not only improved the 2D layered morphology and electrical conductivity but also facilitated enhanced redox activity, accelerated e^- transfer and enhanced structural stability. In addition, the incorporation of MXene significantly increased the C_{sc}, extended the cycling life, and improved the EC performance even at high I_{d}. As shown in Fig. 6(e), CS-MXene exhibited superior C_{sc} across a range of I_{d}.

E_{d} and P_{d} are important factors in estimating the EC performance of the prepared electrode materials. These values

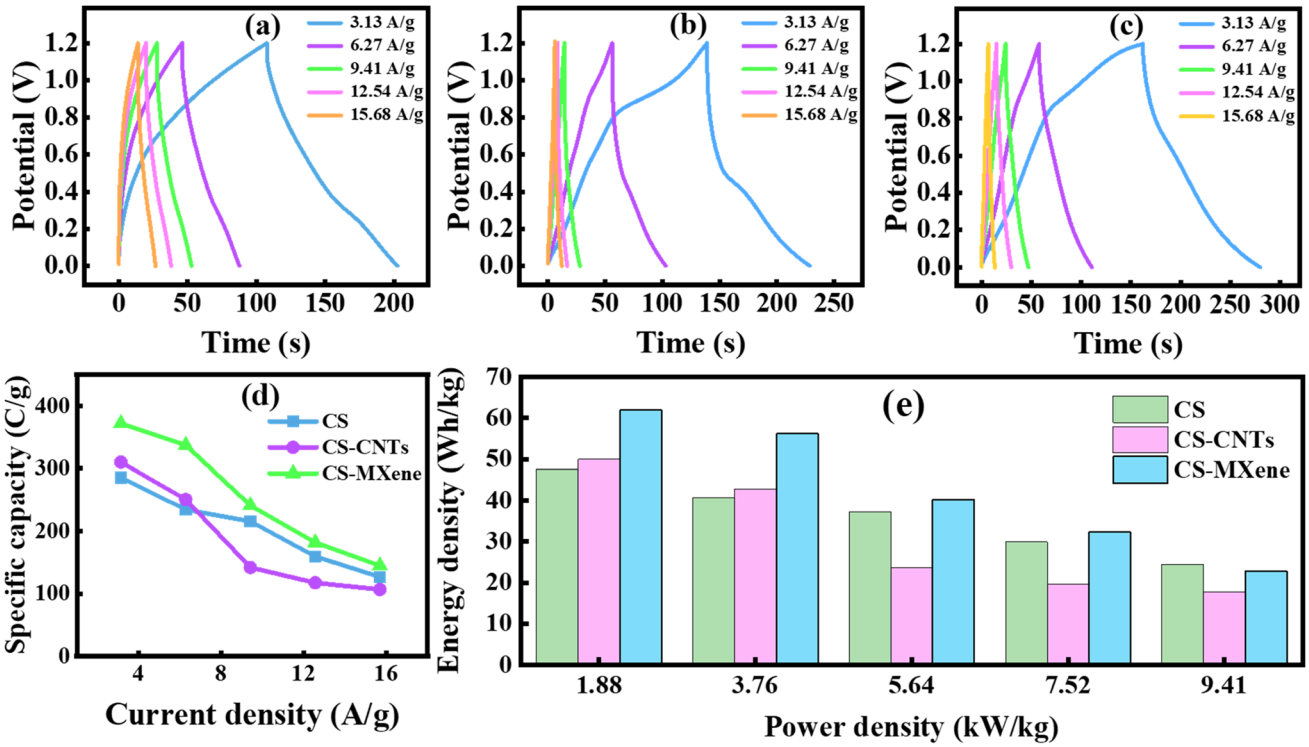

Fig. 7 (a–c) Full cell GCD profiles of CS, CS-CNTs, and CS-MXene, (d) variation of specific capacity with current density, and (e) Ragone plot of all the samples.

were calculated using the formulas $E_d = \frac{\Delta V \times C_p}{2 \times 3.6}$ and $P_d = \frac{E_d \times 3600}{\Delta t}$, and their dependence on I_d is shown in Fig. 6(f). This analysis suggests that the CS-MXene composite, compared to the CS and CS-CNTs composite, demonstrated efficient charge storage capability, contributing to enhancing the overall EC performance. But integrating MXene into pure CS offers excellent charge storage capacity. The electrode achieved an outstanding E_d value of 112.85 Wh kg^{-1} by providing P_d of 1968.50 W kg^{-1}, underscoring the potential used in energy storage applications. The calculated values of E_d and P_d are also given in Table 1.

To evaluate the practical applicability of the fabricated electrodes, a full-cell EC evaluation was conducted, where CS, CS-CNTs, and CS-MXene materials served as anodes and carbon was used as the cathode. The GCD calculations for all the prepared electrodes were performed within a potential range of 0–1.2 V at different I_d to determine the energy storage capability. The enhanced potential window is attributed to the full-cell assembly, where both electrodes operate complementarily; as a result, the cell voltage becomes the sum of individual potentials.[32]

Fig. 7(a–c) displays the GCD profiles for all the electrode materials exhibiting symmetrical triangular profiles with minor fluctuation, confirming the existence of charge storage mechanisms (faradaic and non-faradic), reversibility, and stability of the electrode materials. Fig. 7(a) shows the GCD profiles of pure CS with the C_{sc} measured as 285.27C g^{-1} at I_d of 3.13. These

Table 2 Specific capacity, energy density, and power density of the CS, CS-CNTs and CS-MXene materials from the full-cell GCD analysis

Sample	Current density, (A g^{-1})	Discharge time, (s)	Specific capacity, (C g^{-1})	Energy density, (Wh kg^{-1})	Power density, (W kg^{-1})
CS	3.137	90.93	285.27	47.54	1882.35
	6.274	38.95	244.39	40.73	3764.70
	9.411	25.02	235.48	39.24	5647.05
	12.54, 15.68	14.30, 9.340	179.45, 146.50	29.90, 24.41	7529.41, 9411.76
CS-CNTs	3.137	95.59	299.89	49.98	1882.35
	6.274	35.13	220.43	36.73	3764.70
	9.411	15.06	141.74	23.62	5647.05
	12.54, 15.68	9.350, 6.790	117.33, 106.50	19.55, 17.75	7529.41, 9411.76
CS-MXene	3.137	118.46	371.63	61.93	1882.35
	6.274	53.72	337.06	56.17	3764.70
	9.411	12.41	210.91	35.15	5647.05
	12.54, 15.68	14.48, 7.950	181.70, 124.70	30.28, 20.78	7529.41, 9411.76

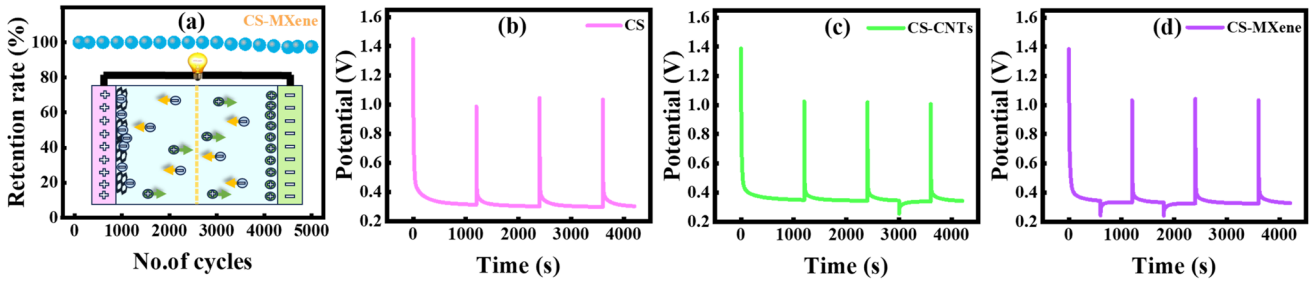

Fig. 8 (a) Retention rate of CS-MXene, (b–d) GITT profiles of CS, CS-CNTs, and CS-MXene.

types of studies have been reported in the literature, where the I_d used for half-cell and full-cell configurations differ significantly. These variations arise from the different charge storage mechanisms and operational mechanisms of the two systems, as a full cell requires optimization of both electrodes to achieve balanced and optimized results.[50] The composite CS-CNTs achieved a quite higher C_{sc} of 299.89C g^{-1} at a similar I_d. Notably, the MXene integrated samples showed the highest C_{sc} of 371.63C g^{-1} at the same I_d. A noticeable decrease in discharge time was observed with an increase in I_d, which is attributed to the least residence time for the ions at the E/E interface. At higher I_d, ions have insufficient time to diffuse into the EC active sites and instead accumulate at the surface, forming a loosely bound layer. These surface-bound ions can be readily extracted, requiring less time compared to ions that penetrate deeper into the electrode material at lower I_d. Fig. 7(d and e) shows the variation of C_{sc} and Ragone plot, which compares the E_d and P_d at different I_d. The fabricated electrodes demonstrated excellent E_d and P_d values, which are highly desirable for energy storage applications. Among all electrodes, CS-MXene exhibited the highest E_d of 61.93 Wh kg^{-1} and P_d 1882 W kg^{-1} values at I_d of 3.13 A g^{-1}. All the calculated values of E_d and P_d are summarized in the accompanying Table 2.

To determine cyclic stability, a two-electrode configuration test was performed, as shown in Fig. 8(a). The CS-MXene composite retained 95.5% of its initial capacity after 5000 charge–discharge cycles, demonstrating outstanding long-term stability. This remarkable performance is attributed to the structural integrity and superior conductivity imparted by the MXene, which mitigates degradation during prolonged cycling. Overall, these results confirmed that the Fe-NS/MXene is a promising electrode material for high-performance energy storage devices due to its exceptional C_{sc}, E_d, P_d, and cyclic life.

4.8 Galvanostatic intermittent titration technique

GITT analysis was employed to investigate the chemical diffusion kinetics of the electrode material by determining the

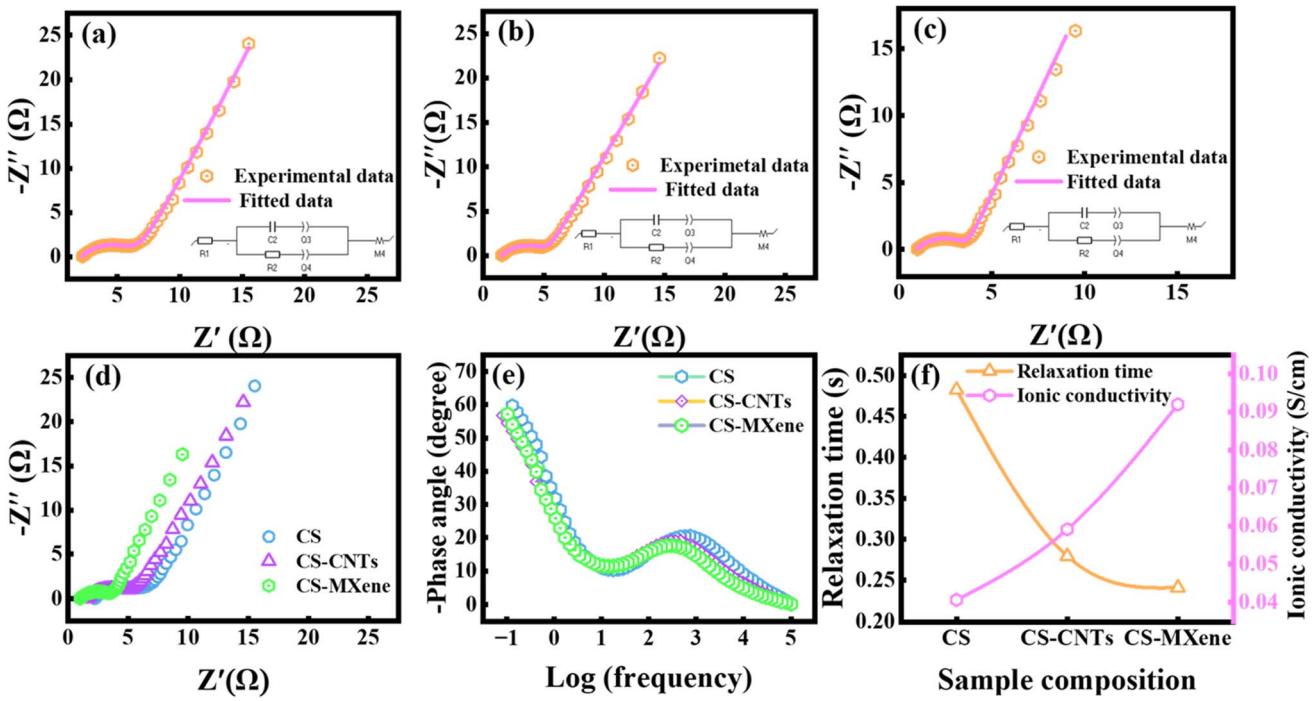

Fig. 9 (a–c) EIS curves fitted spectra of NS, Co-NS, Co-NS/CNTs, and Co-NS/MXene with the appropriate Randle circuit using EC Lab software, (d) Nyquist plot of all the prepared samples, (e) Bode plot of all the synthesized electrode materials, and (f) variation of ionic conductivity and relaxation time for all samples.

diffusion coefficient (D_c). In this method, a constant current pulse was applied to the EC cell for a predetermined time duration, inducing ion adsorption/desorption at the E/E interface.[54,55] During the whole GITT measurement, the variations in voltage and relaxation time were recorded, which were further used for the calculation of D_c. Weppner and Huggins were two scientists who first used the GITT technique in 1997 to find the D_c of synthesized electrode material.[56] The D_c can be calculated with the help of the following eqn (7).

$$D_c = \frac{4}{\pi\tau}\left(\frac{m_B V_M}{M_B S}\right)^2 \left(\frac{\Delta E_S}{\Delta E_\tau}\right)^2 \quad (7)$$

In the above equation, D_c represents the diffusion constant in $cm^2\ s^{-1}$, the molar volume of the prepared sample is denoted by V_M, E/E contact area is symbolized by S, τ shows relaxation time, m_B represents the mass of electrode material, while M_B is the molar mass and ΔE_S and ΔE_τ values are obtained from the graph. In the present research work, GITT measurements were performed for all synthesized samples using a constant current of 1 mA and a fixed charging time of 10 min, having a voltage window range between 0.4 to 1.0 V, as shown in Fig. 8(b–d). For the pristine CS sample, the calculated D_c was found to be $4.58 \times 10^{-11}\ cm^2\ s^{-1}$. In the CS-CNTs, the D_c value increased to $6.32 \times 10^{-11}\ cm^2\ s^{-1}$, which is attributed to the incorporation of CNTs. This is likely due to improved ion diffusion, more efficient charge transfer, and modification of the EC active sites facilitated by the conductive CNT network. For the CS-MXene, the calculated D_c was $5.27 \times 10^{-11}\ cm^2\ s^{-1}$, which is slightly lower than CS-CNTs. This difference is associated with the morphological capabilities of the incorporated materials. CNTs with a porous structure offer an open framework that facilitates faster ion diffusion. In contrast, the 2D layered structure of MXene leads to the formation of densely packed layers, which partially hinder ion transport within the electrode material. In comparison, CNTs typically exhibit a more uniform and well-dispersed network, enhancing overall ion mobility.

4.9 Electrochemical impedance spectroscopy

The EIS analysis was further used to investigate the reaction kinetics and the resistance kinetics of the synthesized samples. The data obtained from EIS analysis of the synthesized samples were plotted as a Nyquist plot. The Nyquist plot typically consists of three distinct regions: high frequency region, which is associated to solution resistance (R_{sr}); the intermediate frequency region, represented by a semicircular arc, which reflects the charge transfer resistance (R_{ctr}) as well as interfacial reaction kinetics; and the low frequency region, characterized by a sloped line (M_a), which is associated with the ion diffusion process within the electrode material.[57–59] In the present context, the frequency range from 10^{-2} to 10^5 Hz was taken for the EIS plot. An explicit pattern of semicircular shape at moderate frequency range, as well as a straight sloped line at low frequency range, was recorded in the curve fitting in the Nyquist plot for the samples CS, CS-CNTs, and CS-MXene, as shown in Fig. 9(a–c). The curve fitting plots were used to get the information about the R_{sr} as well as the R_{ctr}. The R_{sr} values for CS, CS-CNTs, and CS-MXene were calculated as 2.1, 1.5, and 0.9 Ω, respectively, based on the curve fitting shown in Fig. 9(a–c). While EIS curve fitting displayed that the samples CS, CS-CNTs, and CS-MXene exhibited R_{ctr} of 4.4, 4.0, and 2.8 Ω, respectively. These values indicate that CS-MXene possessed both a low R_{sr} as well as R_{ctr}, which facilitates improved ion diffusion and consequently the highest C_{sc} among all prepared samples. The incorporation of CNTs into CS led to a significant improvement in reaction kinetics, porosity, and electrical conductivity, which in turn contributed to a reduction in both R_{sr} as well as R_{ctr}, as given in Table 3. Similarly, the assimilation of MXene into CS enhanced the active surface area of the synthesized electrode material, thereby improving E/E interface contact, stabilizing interfacial charge transfer kinetics, and promoting a more capacitive charge storage behavior. These improvements collectively resulted in a further decrease in R_{sr} and R_{ctr}, ultimately boosting the EC performance of the composite. Fig. 9(d) presents the Nyquist plot for all synthesized samples. A progressive increase in the slope of the low-frequency region from CS to CS-MXene indicates enhanced capacitive behavior, in agreement with the predications of the Dunn model.

Table 3 Values of elements for the corresponding fitted circuit, $R_1 = R_s$, $R_2 = R_{ct}$, Q_2 = constant phase elements, and M_a = restricted diffusion element

Sample	R_1, (Ω)	R_2, (Ω)	Q_2, ($Fs^{(a-1)}$)	Ma, (Ω)
CS	2.12	4.41	0.013	0.68
CS-CNTs	1.52	4.06	0.014	0.38
CS-MXene	0.98	2.78	0.017	0.28

The Bode plot, depicts the negative of the phase angle on the y-axis as a function of the log of frequency on the x-axis. This plot is commonly employed to evaluate the relaxation time and to analyze the frequency-dependent behavior of the charge storage in the prepared electrode material.[60] In general, a phase angle approaching −90° indicates ideal capacitive behavior, whereas a phase angle around −45° is characteristic of pseudocapacitive behavior.[61] The relaxation time can be computed using the following eqn (8).

$$\tau = \frac{1}{2\pi f} \quad (8)$$

In the above equation, relaxation time is denoted by τ, while frequency is represented by f. The relaxation times were calculated for CS, CS-CNTs, and CS-MXene to be 0.32, 0.25, and

Table 4 Calculated values of relaxation time, conductivity and diffusion coefficient

Sample	Frequency (Hz)	Relaxation time (s)	Conductivity ($S\ cm^{-1}$)	Diffusion coefficient ($cm^2\ s^{-1}$)
CS	0.33	0.48	4.1×10^{-2}	4.5×10^{-11}
CS-CNTs	0.57	0.28	5.9×10^{-2}	6.3×10^{-11}
CS-MXene	0.66	0.24	9.2×10^{-2}	5.2×10^{-11}

Table 5 A comprehensive comparison of full and half-cell literature reports, synthesis methodologies, and electrochemical performance metrics of analogous electrode materials

Composition	Method	C_{sc}, P_d, E_d	Diffusion coefficient ($cm^2\ s^{-1}$)	Cyclic stability (%)	Reference
CuS/rGO	Solvothermal	2317.8 F g^{-1}, (1.0 A g^{-1}) (3-E)	N/A	96.2% (1200) cycles	63
CuS/MWCNTs	Hydrothermal	2831 F g^{-1} (1 A g^{-1}) (2-E)	N/A	90% (600) cycles	64
Cu_2S	Hydrothermal	442.2 F g^{-1}, 25.4 Wh kg^{-1}, 4.1 kW kg^{-1} at 1 A g^{-1} (3-E), 93.8 F g^{-1}, 18.6 Wh kg^{-1}, 681.2 W kg^{-1} at 1 A g^{-1} (2-E)	N/A	87% (6k) cycles	65
Ni_9S_8	Hydrothermal	952C g^{-1}, 66.1 Wh kg^{-1}, 2941.2 W kg^{-1} at 11.8 A g^{-1} (3-E), 104.2C g^{-1}, 17.3 Wh kg^{-1}, 423.5 W kg^{-1} at 0.7 A g^{-1} (2-E)	N/A	98.6% (3k)	66
CuS/Ti_3C_2	Hydrothermal	169.5C g^{-1}, 15.4 Wh kg^{-1}, 750.2 W kg^{-1}, at 1 A g^{-1} (2-E)	N/A	82.4% (5k) cycles	67
$NiCoS_4$/MXene	Hydrothermal	396.69C g^{-1}, 27.2 Wh kg^{-1}, 0.48 kW kg^{-1} at 1 A g^{-1} (2 E)	N/A	80% (3k) cycles	68
Cu_2S/MXene	Solvothermal	1692C g^{-1}, 112 Wh kg^{-1}, 2823.52 W kg^{-1}, at 11.7 A g^{-1} (3-E), 371.63C g^{-1}, 61.93 Wh kg^{-1}, 1882 W kg^{-1} at 3.13 A g^{-1} (2-E)	6.32×10^{-11} $cm^2\ s^{-1}$	97.5% (5k) cycles	This work

0.24 s, respectively, as displayed in Fig. 8(f). It was observed that the CS-CNTs exhibited a shorter relaxation time compared to pristine CS, primarily due to the enhanced charge carrier mobility facilitated by the conductive CNT network, which accelerates EC response. Notably, the CS-MXene composite demonstrated the lowest relaxation time among all samples, as demonstrated in Table 4. This improvement is due to the synergistic interaction between MXene and the flower-like morphology of CS, which collectively contribute to an increased surface area and a greater number of EC active sites for redox reactions. The availability of more active sites leads to a reduction in R_{sr} as well as R_{ctr} and promotes faster charge transfer kinetics, thereby significantly lowering the relaxation time.

Ionic conductivity provides critical insight into the ion transport efficiency within the electrolyte medium and reflects the overall EC performance of the system. The ionic conductivity of all synthesized samples was computed with the help following eqn (9).

$$\sigma = \frac{L}{A \times R_{sr}} \tag{9}$$

In the above equation, σ (S cm^{-1}) denotes ionic conductivity, L (cm) represents electrode thickness, A (cm^2) is the electrode area, while R_{sr} (Ω) symbolizes solution resistance.[62] Table 4 presents the calculated ionic conductivity values for CS, CS-CNTs, and CS-MXene, which were determined to be 0.040, 0.059, and 0.092 S cm^{-1}, respectively, as illustrated in Fig. 8(f). Among all samples, CS-MXene efficiently reduces both the R_{sr} and R_{ctr}. The resulting decrease in resistance facilitates improved ion transport throughout the electrolyte, thereby leading to superior ionic conductivity and EC feature for advanced hybrid supercapacitors. Additionally, Table 5 provides a comprehensive comparison with literature-reported materials of a similar kind was carried out to provide a better understanding of the performance.

5. Conclusion

In conclusion, CS and its variants were successfully synthesized through a hydrothermal process followed by solvothermal treatment. The XRD analysis confirmed the formation of an orthorhombic crystal structure, while SEM images revealed a distinct flower-like morphology providing abundant EC active sites. The BET analysis showed an enhanced surface area of 64.18 $m^2\ g^{-1}$ for the CS-MXene composite. Following a comprehensive EC evaluation, the CS-MXene composite demonstrated an outstanding C_{sc} of 1692C g^{-1}, a notable E_d of 112 Wh kg^{-1} in half cell device. Upon full cell assembly, the composite delivered a C_{sc} of 371.63C g^{-1} at I_d of 3.13 A g^{-1}, along with E_d of 61.93 Wh kg^{-1} at P_d of 1882.35. Furthermore, the electrode material retained exceptional cycling stability with 97.5% of its initial capacity after 5000 consecutive charge/discharge cycles. EIS analysis revealed a significant reduction in R_{sr} from 2.21 to 0.97 Ω and a decrement in the R_{ctr} from 4.417 to 2.878 Ω, attributed to high ionic conductivity imparted by the CNTs/MXene integration. Moreover, GITT analysis revealed a maximum diffusion constant of 6.32×10^{-11} $cm^2\ s^{-1}$ for the CS/CNTs composite, ascribed to the blastic ion transport properties of CNTs. These findings underscore the potential of these materials as high-performance electrodes and offer a strategic direction for the development of advanced supercapacitor materials to address contemporary energy demands.

Conflicts of interest

The authors declare that there are no financial or any other types of conflicts of interest to declare for this submission.

Data availability

Data will be made available on request.

Acknowledgements

The authors would like to acknowledge Ongoing Research Funding Program, (ORF-2025-43), King Saud University, Riyadh, Saudi Arabia.

References

1 E. Shahveran and H. Yousefi, *Renew. Sustain. Energy Transit.*, 2025, **7**, 100102.
2 L. J. Ma, J. Xu, J. Wang, J. Jia and H. S. Wu, *Int. J. Hydrogen Energy*, 2025, **140**, 215–222.
3 A. Muzaffar, M. B. Ahamed and C. M. Hussain, *Renewable Sustainable Energy Rev.*, 2024, **195**, 114324.
4 A. H. Tariq, S. A. A. Kazmi, M. Hassan, S. M. Ali and M. Anwar, *Int. J. Hydrogen Energy*, 2024, **52**, 1005–1034.
5 Y. A. Kumar, N. Roy, T. Ramachandran, M. Hussien, M. Moniruzzaman and S. W. Joo, *J. Energy Storage*, 2024, **98**, 113040.
6 H. R. Khan and A. L. Ahmad, *J. Ind. Eng. Chem.*, 2025, **141**, 46–66.
7 Z. Huang, W. Zhou, M. Hu, M. Zhang, X. Zhao, Y. Li, X. H. D. Li and J. Xu, *Chem. Eng. J.*, 2024, **494**, 152907.
8 D. Yadav and N. Srivastava, *J. Power Sources*, 2025, **647**, 237353.
9 C. Han, D. Zhao, C. Tian, T. Li, B. Du, Z. Xu and Y. J. Sui, *J. Alloys Compd.*, 2025, **1046**, 184836.
10 K. Dissanayake and D. Kularatna-Abeywardana, *J. Energy Storage*, 2024, **96**, 112563.
11 S. Lee, S. Kim, Y. R. Jo, B. Im, D. G. Kim, J. Y. Jeon, S. Yang and G. H. An, *J. Alloys Compd.*, 2025, **1036**, 181961.
12 H. Heo, J. Lee, Y. R. Jo and G. H. An, *Adv. Energy Mater.*, 2025, **15**, 2500261.
13 S. Kim, J. Baek, J. I. Choi, Y. R. Jo, S. S. Jang and G. H. An, *Nano Energy*, 2025, **142**, 111203.
14 S. Kim and S. Ju, *J. Energy Chem.*, 2025, **111**, 237–248.
15 M. Riaz, S. M. Ali, N. Bano, S. D. Ali and J. Ullah, *J. Electron. Mater.*, 2025, **54**, 1177–1185.
16 J. B. Mirzanlou, S. M. Masoudpanah, X. Liu, M. S. Bafghi and C. K. Ong, *J. Energy Storage*, 2022, **45**, 103781.
17 A. Das, A. Maitra, A. Mondal, A. De, P. Maity and B. B. Khatua, *J. Energy Storage*, 2024, **92**, 112293.
18 L. Duan, H. Fu, H. Sun, Y. Sun, Z. Lu and J. Liu, *J. Colloid Interface Sci.*, 2024, **676**, 331–342.
19 Q. Tian, Y. Chen, Z. Yang, H. Zhang, Y. Hou and J. Guo, *J. Alloys Compd.*, 2024, **1006**, 176296.
20 L. Rani and J. I. Han, *J. Energy Storage*, 2024, **82**, 110533.
21 J. Chai, G. Wang, G. Wang, R. Shao, J. Zhao, G. Zhao and C. B. Park, *Adv. Funct. Mater.*, 2025, **35**, 2416428.
22 H. Kolavada, R. S. Shukla, P. N. Gajjar and S. K. Gupta, *J. Power Sources*, 2025, **626**, 235796.
23 T. Zahra, I. Barsoum, F. F. Alharbi, Z. Ahmad, H. H. Somaily, M. Abdullah, H. Alqurashi, I. A. Weinstein, A. M. A. Henaish and H. M. T. Farid, *J. Energy Storage*, 2024, **87**, 111470.
24 C. Y. Lee, K. W. Sung and H. J. Ahn, *J. Energy Storage*, 2025, **109**, 115064.
25 A. N. Nabeel, A. Jain, S. K. Arora and E. Nizeyimana, *Int. J. Electrochem.*, 2025, **2025**, 3179088.
26 J. Sun, Y. Mei, W. Bai, L. Han, Y. Li, Y. Gao, M. F. Lang and H. Xue, *Chem. Eng. J.*, 2025, **507**, 160790.
27 A. Feng, Y. Yu, Y. Wang, F. Jiang, Y. Yu, L. Mi and L. Song, *Mater. Des.*, 2017, **114**, 161–166.
28 R. B. Sonpir, D. V. Dake, N. D. Raskar, V. A. Mane, S. S. Shinde, S. S. Ingole, M. S. Tak and B. N. Dole, *Phys. Status Solidi A*, 2025, **222**, 2400502.
29 A. Kumar, A. Yadav and M. Bag, *J. Power Sources*, 2025, **641**, 236825.
30 M. Agrawal and R. T. Durai Prabhakaran, *Polym. Compos.*, 2025, **46**, 1815–1831.
31 P. G. Pawar, B. Pandit, A. M. Al-Enizi, S. H. Sutar, H. M. Pathan, S. H. Mujawar and S. J. Pawar, *Mater. Sci. Eng., B*, 2025, **316**, 118118.
32 G. Khan, M. Luqman, M. Mehak, M. U. Salman, A. Mahmood, W. Al-Masry, M. Nawaz and S. Atiq, *J. Power Sources*, 2025, **660**, 238568.
33 A. Iqbal, R. Nadeem, A. Shakoor, M. Luqman, M. Mehak, M. U. Salman, S. M. Ramay, F. Ahmed and S. Atiq, *J. Energy Storage*, 2025, **134**, 118207.
34 F. M. Ojo, E. Vendemiatti, J. L. Júnior, M. Kumar-Mahto, V. A. Benedito and A. R. G. Simões, *Sci. Rep.*, 2025, **15**, 15292.
35 N. Shaheen, S. Zulfiqar, M. E. El Sayed, A. Samir, M. Shahid, M. F. Warsi and E. W. Cochran, *J. Alloys Compd.*, 2025, **1010**, 178072.
36 M. Ikram, M. M. Baig, I. Shakir, A. Irshad, Z. A. ALOthman, M. F. Warsi and S. G. Lee, *J. Energy Storage*, 2024, **90**, 111746.
37 H. Yaldiz, A. C. Kocal, O. Gultepe, E. Gür and F. Atay, *Electrochim. Acta*, 2025, **526**, 146197.
38 S. Seenivasan, A. T. Sivagurunathan and D. H. Kim, *Energy Storage Mater.*, 2024, **70**, 103482.
39 X. Yin, W. Zheng, H. Tang, L. Yang, C. Lu, L. Pan, P. Zhang and Z. Sun, *Energy Storage Mater.*, 2024, **72**, 103688.
40 M. N. Ramadhasan, M. Ragam and S. J. Selvasekarapandian, *J. Electroanal. Chem.*, 2025, **983**, 119011.
41 P. A. Shinde, Y. Seo, S. Lee, H. Kim, Q. N. Pham, Y. Won and S. C. Jun, *Chem. Eng. J.*, 2020, **387**, 122982.
42 X. He, Y. Hu, H. Tian, Z. Li, P. Huang, J. Jiang and C. Wang, *J. Materiomics*, 2020, **6**, 192–199.
43 D. Roy, R. Kedia, A. Patra and K. Deori, *ACS Appl. Polym. Mater.*, 2025, **7**, 7811–7823, https://pubs.acs.org/doi/full/10.1021/acsapm.5c00478.
44 P. Bhojane, *J. Energy Storage*, 2022, **45**, 103654.
45 B. Bari, P. Tyagi and U. Udeochu, *Sci. Rep.*, 2025, **15**, 13365.
46 V. Selvanathan, M. Rokonuzzaman, S. A. Razali, P. Chelvanathan, M. A. Islam, M. S. Suait, Md. Akhtaruzzaman and T. S. Kiong, *Int. J. Energy Res.*, 2025, **2025**, 8895957.
47 R. Hasan, Y. Altaf, N. Jabeen, N. U. Hassan, F. Ahmed, S. Hussain, A. Hussain, S. U. Asif and B. A. Al-Asbahi, *J. Electroanal. Chem.*, 2024, **966**, 118411.
48 K. M. Albalawi, M. Al-Dossari, A. M. Saeedi, R. H. Althomali, G. F. Solre, M. Sadiq and S. U. Asif, *J. Energy Storage*, 2024, **104**, 114576.

49 A. Ray, A. Roy, M. Ghosh, J. A. Ramos-Ramón, S. Saha, U. Pal, S. K. Bhattacharya and S. Das, *Appl. Surf. Sci.*, 2019, **463**, 513–525.
50 M. Luqman, M. Mehak, M. U. Salman, A. Raza, S. M. Ramay, M. Younis and S. Atiq, *J. Power Sources*, 2025, **655**, 237943.
51 R. Lan, E. Gkanas, A. J. S. Sahib, A. Greszta, R. Bhagat and A. Roberts, *J. Alloys Compd.*, 2024, **992**, 174528.
52 S. Jadhav, R. S. Kalubarme, N. Suzuki, C. Terashima, B. Kale, S. W. Gosavi, M. Ashokkumar and A. Fujishima, *Surf. Coat. Technol.*, 2021, **419**, 127287.
53 M. Mehak, M. Luqman, M. U. Salman, A. Ahmad, S. M. Ramay, M. Younis and S. Atiq, *J. Mater. Chem. C*, 2025, **37**, 19067–19492.
54 E. Deiss, *Electrochim. Acta*, 2005, **50**, 2927–2932.
55 T. Schied, A. Nickol, C. Heubner, M. Schneider, A. Michaelis, M. Bobeth and G. Cuniberti, *ChemPhysChem*, 2021, **22**, 885–893.
56 J. Sun, S. Sun, X. Yang, F. Xie and Z. Shao, *Appl. Energy*, 2025, **381**, 125111.
57 R. F. Shiraz, M. Mozammel, S. M. Emarati, R. Jafari and A. Safari, *Adv. Mater. Interfaces*, 2025, **12**, 2400616.
58 J. Kim, S. Park, S. Hwang and W. J. Yoon, *J. Electrochem. Sci. Technol.*, 2022, **13**, 19–31.
59 Y. Li, L. Ni, J. Luo, L. Zhu, X. Zhang, H. Li, I. Zada, J. Yu. S. Zhu, K. Lian, Y. Li and D. Zhang, *Adv. Funct. Mater.*, 2024, **34**, 2403448.
60 H. N. Abdelhamid, *Appl. Organomet. Chem.*, 2025, **39**, e70193.
61 V. K. Mariappan, K. Krishnamoorthy, P. Pazhamalai, S. Sahoo and S. J. Kim, *Electrochim. Acta*, 2028, **265**, 514–522.
62 S. Wang, C. Li, Y. Ma, H. Zhang, X. Shi, L. Zhang and D. Song, *Angew. Chem.*, 2025, **137**, e202420698.
63 K. J. Huang, J. Z. Zhang, Y. Liu and Y. M. Liu, *Int. J. Hydrogen Energy*, 2015, **40**, 10158–10167.
64 K. J. Huang, J. Z. Zhang and K. Xing, *Electrochim. Acta*, 2014, **149**, 28–33.
65 T. Zhao, X. Peng, X. Zhao, J. Hu, W. Yang, T. Li and I. Ahmad, *Composites, Part B*, 2019, **163**, 26–35.
66 M. Luqman, M. Mehak, M. U. Salman, S. M. Ramay, M. Younis and S. Atiq, *Appl. Phys. Lett.*, 2025, **127**, 083901.
67 Z. Pan, F. Cao, X. Hu and X. Ji, *J. Mater. Chem. A*, 2019, **7**, 8984–8992.
68 H. Li, X. Chen, E. Zalnezhad, K. N. Hui, K. S. Hui and M. J. Ko, *J. Ind. Eng. Chem.*, 2020, **82**, 309–316.